Ocean Modelling 69 (2013) 93–107

Contents lists available at SciVerse ScienceDirect

Ocean Modelling

journal homepage: www.elsevier.com/locate/ocemod

A higher order discontinuous Galerkin, global shallow water model: Global ocean tides and aquaplanet benchmarks

H. Salehipour *, G.R. Stuhne, W.R. Peltier

Physics Department, University of Toronto, 60 St. George St., Toronto, Ontario M5S 1A7, Canada

ARTICLE INFO

Article history:
Received 6 February 2013
Received in revised form 17 May 2013
Accepted 6 June 2013
Available online 20 June 2013

Keywords:
Discontinuous Galerkin
Global oceanic tides
Tide modeling
Shallow water equation
Unstructured grids
Parallel computing

ABSTRACT

The development of models of the ocean tides with higher resolution near coastlines and coarser resolution offshore, has been required to account for the significant impacts of coastline configuration and bathymetry (associated with sea level rise) on both the amplitude and phase of tidal constituents. This capability becomes especially important in the context of tidal analyses at times in the past when sea levels are known to have differed significantly from present. Here we present a novel global model based on the discontinuous Galerkin disretization of the shallow water equations that employs third order Runge–Kutta time stepping on unstructured triangular grids. The model has been efficiently parallelized and is thereby shown to achieve essentially perfect linear scaling which makes it suitable for the generation of extremely high resolution results in local regions of interest.

The paper includes a detailed development of the mathematical and numerical framework which is first tested in the context of analyses of a series of well established aquaplanet benchmarks for the shallow water equations on the sphere. These benchmarks include: (1) steady state nonlinear geostrophic flow in the context of an *hp* convergence study, (2) Rossby wave response arising from a geostrophic flow impinging on localized topography and (3) development of barotropic instability in a perturbed balanced zonal flow. For our target tidal applications the basic shallow water system is extended to include the influence of internal tide-related drag in the deep ocean as well as the drag in shallow marginal seas together with the influence of gravitational self-attraction and loading. Global tidal simulations with various offshore and coastal resolutions are compared with the standard benchmark based upon satellite altimetry data. Initial investigations of the M_2 tidal amplitude, phase and energy budget are provided and shown to be highly satisfactory at the level of resolution for which results are provided.

1. Introduction

Modeling of global ocean tides has experienced a resurgence of interest over the past decade due to increasing recognition of the critical role played by the dissipation of the barotropic tidal flow over bottom topography through excitation of internal tides (Garrett and Kunze, 2007). This interaction is known to contribute significantly to the energy budget of the tide and contribute critically to the establishment of the spatial distribution of the turbulent diapycnal diffusivities that arise as a consequence of small scale ocean mixing processes (Munk and Wunsch, 1998).

The amplitude and phase of individual tidal constituents are also significantly impacted by sea level rise and the associated variations in coastline configurations and ocean bathymetry, not only under modern global warming conditions but also in the deep past (Griffiths and Peltier, 2008; Griffiths and Peltier, 2009; Egbert et al., 2004; Uehara et al., 2006). In order to better address all of these issues, an improved global model of ocean tides is expected to be a useful tool, especially if based upon modern numerical methodologies that are able to make full use of existing computational capability.

Barotropic oceanic tides have been traditionally modeled using one or the other of the following three distinct methodologies:

1. Globally structured Arakawa C-grid models by using conventional second order centred finite differences (Egbert et al., 2004; Arbic et al., 2004) or invoking a rotation of the poles of the spherical polar coordinate system as in Griffiths and Peltier (2008); Griffiths and Peltier (2009) so as to enable high resolution near the poles and avoid the geometrical singularity at the poles.
2. Globally unstructured triangular grids with local refinements based on use of a finite volume scheme (Stuhne and Peltier, 2009) or a finite element approach (Le Provost et al., 1994, Lyard, 1997, Lyard et al., 2006).

* Corresponding author. Tel.: +1 416 946 3019.
E-mail address: h.salehipour@utoronto.ca (H. Salehipour).

1463-5003/$ - see front matter © 2013 Elsevier Ltd. All rights reserved.
http://dx.doi.org/10.1016/j.ocemod.2013.06.001

3. Hybrid methods (nested modeling) as in Hill et al. (2011) where a global model with coarse resolution is employed to provide the "open" boundary conditions required by a separate regional model.

Globally structured grid-based tidal simulations in a conventional spherical polar coordinate system, not only suffer from the polar singularity problem, but are incapable of locally resolving the coastlines or arbitrary regions of interest, without imposing a global refinement of the mesh and hence unacceptable computational cost. Unstructured grids on the other hand, provide a superior alternative, enabling selective focus upon specific regions of interest such as topographic features in the deep ocean or coastal shelves and estuaries. Insofar as the third of the above mentioned methodologies is concerned, in which a high resolution local model of one design is nested within a low resolution model of a perhaps different design, this strategy relies upon the quality of the open boundary conditions provided by the global model when applied to drive that nested within it. The correct prescription of the open boundary conditions is challenging (Logutov and Lermusiaux, 2008), however, and noticeably affects the estimation of regional high-resolution tides (Carter and Merrifield, 2007). The availability of a standalone framework which can be employed to study highly resolved regions without relying on secondary models would therefor be extremely useful for a number of modern problems in which high resolution local information concerning tidal constituents is required that does not rely upon having the open boundary condition information being provided by an additional model. The search for an appropriate compromise between numerical accuracy, flexibility and efficiency must be the main driver for selection of the discretization scheme in a tidal model. In contrast to finite difference methods, finite element (continuous Galerkin) and finite volume methods share an important robustness in their ability to represent complex computational domains based on triangular tessellation of the sphere as in Stuhne and Peltier (2009) and Lyard et al. (2006). Nevertheless, finite element methods are able to provide higher accuracy on unstructured grids whereas finite volume methodology is preferable insofar as conservation properties are concerned especially in advectively dominated flows (Hesthaven and Warburton, 2008). Furthermore, the computational cost associated with solving tidal hydrodynamics analyses using any of the above discretization schemes, either in the time-domain (Stuhne and Peltier, 2009) or the frequency domain (Griffiths and Peltier, 2008) is prohibitive, alluding to the parallel performance of the desired numerical scheme. All of these facts have led us to the development of our methodology of choice.

A discontinuous Galerkin (DG) discretization of conservation laws, combines all the favorable properties of finite volume and finite element methods (Cockburn and Shu, 1998) making it an ideal choice for tidal simulation. It provides very high orders of accuracy (both in space and time) while ensuring that mass and momentum transports are locally conserved (Giraldo et al., 2002). In addition, DG inherits the flexibility in representing geometrical features using global unstructured grids thus facilitating the use of local spatial refinement. In addition to the above properties and as will be shown in what follows, the DG scheme, provides exceptional scaling properties due to its compact stencil when parallelized even across thousands of individual computer "cores" on a modern commodity cluster.

DG based shallow water models on the sphere have previously been developed in (i) Cartesian coordinates for icosahedral-based quadrilateral (Giraldo et al., 2002) and triangular (Giraldo, 2006) grids (ii) cubed-sphere grids in curvilinear coordinates (Nair et al., 2005; Nair et al., 2005) and (iii) spherical triangular coordinates (Laeuter et al., 2008). There are also several DG-based shallow water models on the f-plane or β-plane such as those by Aizinger and Dawson (2002) and Eskilsson and Sherwin (2004). More recently these methods have been employed in different applications such as: regional studies of hurricane storm surges (Dawson et al., 2011), tidal flows around shallow water islands (Bernard et al., 2009), coastal ocean modeling applications with possible h and p adaptivity (Bernard et al., 2007; Kubatko et al., 2009), and for global tsunami simulations (Blaise and St-Cyr, 2012). None of the previous work, however, has addressed the problem of global tidal simulation which is the focus of the current paper.

In this paper, we present a standalone framework for accurate multi-scale investigation of barotropic tides based on the use of third order Runge–Kutta discontinuous Galerkin discretization of the nonlinear shallow water equations using global icosahedral grids with proper tidal forcing. Section 2 explains the mathematical model and the DG formulation. Section 3, describes our numerical implementation and parallelization algorithm. Several aquaplanet benchmark tests are performed together with a series of global tidal simulations which are presented and discussed in Sections 4 and 5, respectively. We offer a summary and conclusions in Section 6.

2. Shallow water equations and the barotropic tide

Barotropic ocean tides are well represented in terms of 2D spherical shallow water equations (Egbert et al., 2004). The complete forms of these equations required for this application, as discussed for example in Hendershott (1972), will be presented in what follows. Here we will begin by stating the general form of these equations that are employed to describe the dynamics of a thin layer of fluid with depth h on the surface of a sphere, in terms of the geopotential height ($\phi = gh$) in conservation form as follows:

$$\partial_t \phi + \nabla \cdot \phi \mathbf{u} = 0, \tag{1}$$

$$\partial_t(\phi \mathbf{u}) + \nabla \cdot (\phi \mathbf{u}\mathbf{u}) = -f\hat{\mathbf{e}}_g \times (\phi \mathbf{u}) - \phi \nabla(\phi - \phi_s) + \frac{g}{\rho}\mathcal{F}, \tag{2}$$

in which $\phi\mathbf{u}$ is the depth-averaged horizontal transport and $\mathcal{F}$ denotes a general forcing term which is zero for an unforced aquaplanet flow but will be specified for our tidal studies in Section 2.2. Also f is the Coriolis parameter and $\hat{\mathbf{e}}_g$ represents a unit vector, normal to the surface of the sphere pointing in the direction opposite to that of the gravitational acceleration of strength g. As depicted in Fig. 1, the fluid depth is:

$$h(\mathbf{x}, t) = h_s(\mathbf{x}) + \zeta(\mathbf{x}, t) \tag{3}$$

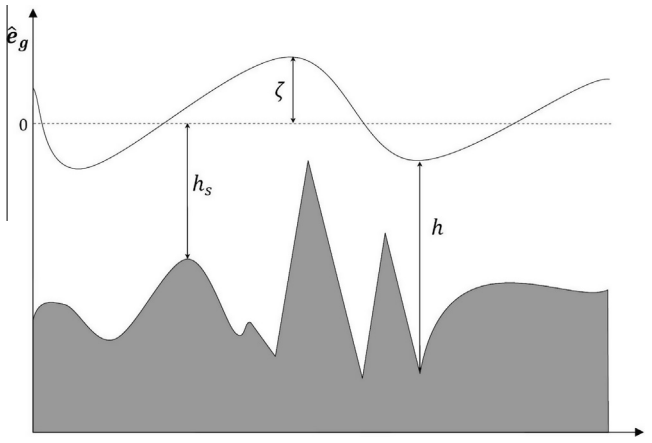

Fig. 1. Definition of water depth (h), bathymetry (h_s) and free-surface elevation ζ in the rotating shallow water equations.

where ζ is the free-surface elevation and h_s denotes the bathymetric depth measured from the undisturbed level of the ocean surface which is assumed to be a gravitational and centrifugal equipotential surface (the geoid of classical geodesy, see Peltier et al. (2012) for a detailed discussion). We will base our model upon the above forms of the shallow water equations in a Cartesian coordinate system located at the origin of the sphere.

2.1. Shallow water in Cartesian coordinates

In the global Cartesian coordinate system, which has been employed in this work, Eqs. (1) and (2), combined as a system of coupled equations, can be written in flux form as follows:

$$\partial_t \mathbf{Q} + \nabla \cdot \mathbf{F}(\mathbf{Q}) = \mathbf{S}(\mathbf{Q}) \tag{4}$$

In this representation, conserved variables are lumped into $\mathbf{Q}(\mathbf{x},t) = [\phi \;\; \phi\mathbf{u}]^T$ and the flux and source terms are denoted by $\mathbf{F}$ and $\mathbf{S}$ respectively which are defined as $\mathbf{F} = [\mathbf{F^x}, \mathbf{F^y}, \mathbf{F^z}]$ with the following components:

$$\mathbf{F^x} = \begin{bmatrix} \phi u \\ \phi u^2 + \frac{1}{2}\phi^2 \\ \phi u v \\ \phi u w \end{bmatrix}, \quad \mathbf{F^y} = \begin{bmatrix} \phi v \\ \phi u y \\ \phi v^2 + \frac{1}{2}\phi^2 \\ \phi v w \end{bmatrix}, \quad \mathbf{F^z} = \begin{bmatrix} \phi w \\ \phi u w \\ \phi v w \\ \phi w^2 + \frac{1}{2}\phi^2 \end{bmatrix} \tag{5}$$

and the components of $\mathbf{S}$ in the absence of tide-related terms are:

$$\mathbf{S} = \begin{bmatrix} 0 \\ f\left(\frac{z}{a}\phi v - \frac{y}{a}\phi w\right) + \phi\phi_{s,x} + \mu x \\ f\left(\frac{x}{a}\phi w - \frac{z}{a}\phi u\right) + \phi\phi_{s,y} + \mu y \\ f\left(\frac{y}{a}\phi u - \frac{x}{a}\phi v\right) + \phi\phi_{s,z} + \mu z \end{bmatrix} \tag{6}$$

In the above equations, Earth's radius is $a = 6.37122 \times 10^6$ m and $\hat{\mathbf{e}}_g = \mathbf{x}/a$. Note that the pressure term $\phi\nabla\phi = \nabla(\frac{1}{2}\phi^2)$ in Eq. (2) has been moved to the flux term in order to cast the governing equations into standard conservation form (Giraldo, 2000). This formulation enables direct analysis of a conservative system based upon the conservation laws themselves.

Because of the additional degree of freedom, acquired by choosing to describe what is a two dimensional motion on the surface of a sphere using a three dimensional global Cartesian coordinate system, the velocity vector $\mathbf{u} = (u, v, w)^T$ must now be explicitly constrained to the surface. As first proposed by Cote (1988), this can be achieved by introducing a force which appears through a Lagrange Multiplier, and is designed to annihilate any tendency of fluid particles to accelerate off this surface. Writing the constrained velocity vector in Cartesian coordinates as $\mathbf{u}^c = \mathbf{u}^u + \mu\mathbf{x}$ (where $\mathbf{u}^u$ is the unconstrained velocity corrected by $\mu\mathbf{x}$ and μ is the Lagrange multiplier), and requiring zero projection along $\mathbf{x}$, one can derive the projection matrix introduced by Williamson et al. (1992) as:

$$\mathbf{u}^c = \mathbf{P}\mathbf{u}^u$$
$$\mathbf{P} = I - \frac{\mathbf{x}^T\mathbf{x}}{a^2} \tag{7}$$

After each stage of the Runge–Kutta time-stepping in the model, the above projection matrix acts on the discretized velocity vector to ensure spherical tangency.

2.2. Tidal forcing

For the simulation of ocean tides, we solve the full nonlinear barotropic shallow water equations as in Eqs. (1) and (2), unlike most of the previous tidal models where the nonlinear advection of horizontal transport in Eq. (2) is omitted (e.g., see Egbert et al., 2004; Griffiths and Peltier, 2008; Griffiths and Peltier, 2009; Lyard et al., 2006). Also $\mathcal{F}$ in Eq. (2) must include momentum sources and sinks associated with tides which leads to the following modified form of Eq. (6) with S redefined as:

$$\mathbf{S} = \left[0, -f\hat{\mathbf{e}}_g \times (\phi\mathbf{u}) + \phi\nabla(\phi_{eq} + \phi_{\text{sal}} - \phi_s) - \frac{g}{\rho}(\mathbf{D}_{\text{BL}} - \mathbf{D}_{\text{IT}})\right]^T \tag{8}$$

in which $\phi_{eq} = g\zeta_{eq}$ and ζ_{eq} is the equilibrium tidal elevation induced by the gravitational field of the Moon or Sun for the specific lunar and solar tides of interest. Periodic expressions of ζ_{eq} encompassing long-period (l), diurnal (d) and semi-diurnal (s) tides can be expressed as.

$$\zeta_{eq} = \sum_l A_l\kappa_l\left(\frac{1}{2} - \frac{3}{2}\sin^2\theta\right)\cos(\omega_l t) + \sum_d A_d\kappa_d \sin(2\theta) \times \cos(\omega_d t + \lambda) + \sum_s A_s\kappa_s\cos^2\theta\cos(\omega_s t + 2\lambda) \tag{9}$$

where θ and λ are latitude and longitude, A is the equilibrium amplitude, ω is the tidal frequency and κ is the appropriate surface load Love number (Farrell et al., 1972; Hendershott, 1972), all of which will be found compiled in (Arbic et al., 2004 Table 2).

The effect of the gravitational self-attraction and loading (SAL) of the tide by the deforming surface of the solid earth is included in $\phi_{\text{sal}} = g\zeta_{\text{sal}}$. The exact representation of ζ_{sal} involves a convolution integral of ζ which turns Eq. (4) into an integro-differential equation which renders the numerical solution computationally challenging (Hendershott, 1972; Ray, 1998). A simplified scalar approximation of $\zeta_{\text{sal}} = \beta\zeta$ (where $\beta = 0.085$ (Accad and Pekeris, 1978)), although crude (Ray, 1998), will suffice in the current paper which focuses on the overall numerical framework. The corresponding pressure terms ($\frac{1}{2}\phi^2$) in Eq. (5) are multiplied by a factor of $(1-\beta)$ as a consequence of this approximation.

The momentum dissipation acting on the tide is represented through parametrization of boundary layer drag D_{BL} and an additional drag induced by an assumed vertically averaged influence of the internal tides D_{IT}. The boundary layer drag is parameterized as per (Taylor, 1919) using the canonical drag coefficient of $c_d = 0.0025$ as:

$$\mathbf{D}_{\text{BL}} = \rho c_d|\mathbf{u}|\mathbf{u}, \quad c_d = 0.0025 \tag{10}$$

Following Griffiths and Grimshaw (2007) and Griffiths and Peltier (2008, 2009), we will parameterize the internal tide drag through the addition of the term:

$$\mathbf{D}_{\text{IT}} = \frac{\rho\overline{N}^2 h_s}{3\omega}(\mathbf{u}\cdot\nabla h_s)\nabla h_s \times \begin{cases} 1 & |f| < \omega \\ 0 & |f| > \omega \end{cases} \tag{11}$$

where f is the Coriolis parameter and $\overline{N}$ is the vertically averaged buoyancy frequency of the ocean which for a single epoch of time is assumed to be a function only of position to be obtained from direct ocean observations under modern conditions or from the predictions of a full coupled atmosphere–ocean climate model for past or future conditions. For the purpose of the results to be shown in the present paper, we have employed the neutral density measurements from WOCE to compute $\overline{N}$ as follows:

$$\overline{N} = \frac{1}{h_s}\int_{-h_s}^{0} N(z)dz \tag{12}$$

This parametrization for the internal tide drag, ensures anisotropy of the drag with respect to bottom topography in the sense that the drag will be zero for flow parallel to bathymetric contours but maximum when the flow is perpendicular to them. There is a strong analogy here with the problem of mountain wave drag associated with the launching of internal waves by the flow of density stratified atmospheric air over high topography (e.g., Peltier and

Clark, 1979, 1983; Peltier and Scinocca, 1990). In addition, there is zero drag for waves that are longer than the inertial wavelength which for M_2 tides translates into latitudes with $|\theta| > 74.5^\circ$.

3. Numerical scheme

The proposed model solves Eq. (4) with proper source terms as in Eqs. (6) or (8), and flux terms as in Eq. (5) on a global spherical triangular tessellation of the surface of the sphere using the nodal DG approach. This section introduces the discretized set of equations, the required local operators, grid generation methodology and parallelization.

3.1. Discontinuous Galerkin spatial discretization

For the spatial discretization of Eq. (4), the spherical computational domain Ω is split into K triangular elements D^k with curvilinear edges (Giraldo, 2006) and the exact solution is approximated by a direct sum of local solutions $Q_h^k(\mathbf{x},t)$ as:

$$\Omega \simeq \Omega_h = \bigcup_{k=1}^{K} D^k, \quad Q(\mathbf{x},t) \simeq Q_h(\mathbf{x},t) = \bigoplus_{k=1}^{K} Q_h^k(\mathbf{x},t)$$

The local discretized solution Q_h^k on each triangular domain D^k, is approximated using a local N^{th} order piecewise polynomial:

$$\mathbf{x} \in D^k: \quad Q_h^k(\mathbf{x},t) = \sum_{i=1}^{N_p} Q_h^k(\mathbf{x}_i^k,t)\ell_i^k(\mathbf{x}), \tag{13}$$

where $\ell_i^k(\mathbf{x})$ is the multidimensional interpolating Lagrange polynomial defined on N_p grid points of the k^{th} element.

3.1.1. Weak DG formulations

Following a general Galerkin approach, the local residual, formed after substituting $Q_h^k(\mathbf{x},t)$ into Eq. (4), must be forced to vanish by requiring it to be orthogonal to all the test functions ψ in a globally defined space of all possible test functions. Integrating the flux term by parts and applying Green's theorem yields the classical formulation of *weak* DG in a local semidiscrete form (Cockburn and Shu, 2002):

$$\int_{D^k}\left[\frac{\partial \mathbf{Q_h}}{\partial t} - \mathcal{I}_N\{\mathbf{F_h}(\mathbf{Q})\}\cdot\nabla - \mathcal{I}_N\{\mathbf{S_h}(\mathbf{Q})\}\right]\psi_i(\mathbf{x})d\mathbf{x} = -\int_{\partial D^k}\mathcal{I}_N\{\mathbf{F_h^*}(\mathbf{Q})\cdot\hat{\mathbf{n}}\}\psi_i(\mathbf{x})d\mathbf{x} \tag{14}$$

where $\hat{\mathbf{n}}$ is the outward-facing normal vector on the element boundary ∂D^k and $\mathcal{I}_N$ indicates the Nth order interpolating operator associated with element nodes as will be precisely specified in Eq. (23) below.

Writing Eq. (14) in a semi-explicit form, where the left-hand side includes only the transient term, the remaining terms in the right-hand side are divided into surface integrals of flux and source terms on D_k as well as an edge integral of the numerical flux (the terms with an asterisk) on ∂D_k as:

$$\begin{aligned}\int_{D^k}\left(\frac{\partial \mathbf{Q}_h}{\partial t}\psi_h\right)d\mathbf{x} = &\int_{D^k}\left(\mathcal{I}_N\{\mathbf{F_h^x}\}\frac{\partial\psi_h}{\partial x} + \mathcal{I}_N\{\mathbf{F_h^y}\}\frac{\partial\psi_h}{\partial y} + \mathcal{I}_N\{\mathbf{F_h^z}\}\frac{\partial\psi_h}{\partial z}\right)d\mathbf{x}\\ &+\int_{\partial D^k}\mathcal{I}_N\{\hat{n}_x\mathbf{F_h^x}+\hat{n}_y\mathbf{F_h^y}+\hat{n}_z\mathbf{F_h^z}\}^*\psi_h d\mathbf{x}\\ &+\int_{D^k}\mathcal{I}_N\{\mathbf{S_h}\}\psi_h d\mathbf{x}\end{aligned} \tag{15}$$

For the nonlinear flux ($\mathbf{F}$) and source ($\mathbf{S}$) terms, aliasing errors would be incurred if one were to use the same Galerkin nodes of the Lagrange polynomial ℓ_i for approximating F_h, similar to the approximation of Q_h in Eq. (13) i.e., $F_h(x,t) = \sum_{i=1}^{N_p} F_h(x_i,t)\ell_i$ (Hesthaven and Warburton, 2008). Our model rather exploits supplementary interpolating nodes such as *cubature* nodes for surface integrals (D^k) and *Gaussian quadrature* nodes for edge integrals (∂D^k) for numerical accuracy.

In the current model, only the weak DG formulation is used for the spatial discretization. The semidiscrete strong DG formulation produces similar results for shallow water equations on the sphere according to Giraldo (2006) and to our knowledge will have no superior numerical performance for the current tidal applications.

3.1.2. Numerical flux

Probably the most striking feature of discontinuous Galerkin, as opposed to continuous Galerkin, is the introduction of *numerical flux* which improves the flow of information, consistent with problem dynamics. In fact, the reconstruction of the elemental interface values is required in DG due to its local definition in terms of polynomial solutions (i.e., the discontinuous formulation) and therefor a lack of a unique solution at interfaces. This concept is borrowed from finite volume literature where the exact and approximate solutions of the Riemann problem are used for such purposes (e.g., Toro, 2001). One simple and widely used (Nair et al., 2005; Giraldo, 2006) method of this kind is *Lax–Friedrichs* or *Rusanov* flux which is also employed in the current work.

The Lax–Friedrichs numerical flux $\mathbf{F}_h^*$ is obtained as:

$$\mathbf{F}_h^* = \frac{\mathbf{F}_h^- + \mathbf{F}_h^+}{2} + \frac{\lambda}{2}(\mathbf{Q}^-\cdot\hat{\mathbf{n}}^- + \mathbf{Q}^+\cdot\hat{\mathbf{n}}^+) \tag{16}$$

in which the "−" and "+" superscripts denote respectively the element interior and exterior information along the interface edge. Also λ is an approximation to the local maximum wave speed which for the shallow water equation is the local fluid speed plus the characteristic gravity wave speed, namely:

$$\lambda = \max\left(|U^-| + \sqrt{\phi^-}, |U^+| + \sqrt{\phi^+}\right)$$

When the local Lax–Friedrichs flux is inserted into Eq. (14), the normal numerical flux (i.e., $\mathbf{F_h^*}(\mathbf{Q})\cdot\hat{\mathbf{n}}$) becomes:

$$\mathbf{F}_h^*\cdot\hat{\mathbf{n}} = \frac{\mathbf{F}_h^-\cdot\hat{\mathbf{n}} + \mathbf{F}_h^+\cdot\hat{\mathbf{n}}}{2} + \frac{\lambda}{2}(\mathbf{Q}^- - \mathbf{Q}^+) \tag{17}$$

The Lax–Friedrichs numerical flux combines an averaging central scheme (the first term in Eq. (16)) with a correction based on the direction of information propagation using normal jumps along the interface edge (the second term including λ).

Once the numerical flux is in place, a unique solution is ensured at the elemental interfaces. Using this scheme, possibly sharp gradients, that may exist for example in the topographic features (as shown schematically in Fig. 1), are handled sufficiently well without smoothing or adding ad hoc diffusion parameters. We consider that this property will prove useful in physical understanding of the numerical results that the model delivers as spatial resolution increases.

3.2. Discontinuous Galerkin local operations

3.2.1. Mapping the physical triangles onto a reference triangle

In order to avoid numerical computations on the physical unstructured triangles on the sphere, a geometric mapping Ψ translates each of the physical triangles $\mathtt{D}$ into a reference triangle $\mathtt{I}$ as depicted in Fig. 2. Following Hesthaven and Warburton (2008) and Giraldo (2006), we define the reference element on a local reference coordinate system (r,s,t) such that:

$$\mathtt{I} = \{(r,s,t), \quad -1 \leqslant (r,s) \leqslant 1, \quad r+s \leqslant 0, \quad t = 1\}$$

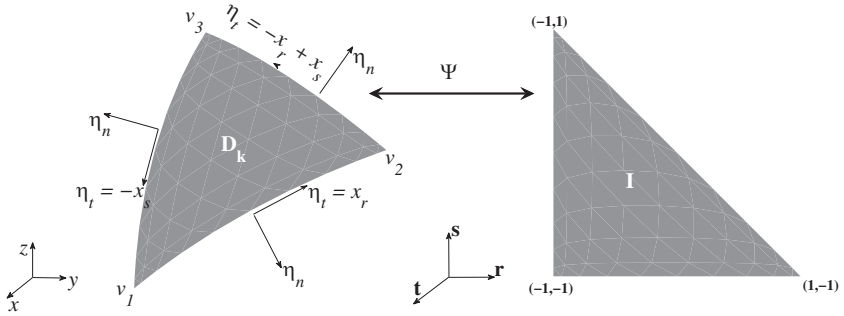

Fig. 2. Mapping from a curvilinear triangle in (x,y,z) coordinates onto the standard triangle in (rs,t) coordinates.

We can express the physical coordinates $\mathbf{x} = (x,y,z)$ in terms of the reference coordinate (r,s,t) using the N_p nodes which corresponds to an Nth order basis function:

$$\mathbf{x} = \sum_{i=1}^{N_p} t\psi_i(r,s)\mathbf{x}_i \tag{18}$$

where $N_p = \frac{1}{2}(N+1)(N+2)$.

The transformation metrics are determined after inverting $J = \frac{\partial \mathbf{x}}{\partial \mathbf{r}}$ and setting it equal to $J^{-1} = \frac{\partial \mathbf{r}}{\partial \mathbf{x}}$ (Giraldo, 2001). Using $t = 1$ the metrics become:

$$\begin{bmatrix} r_x \\ r_y \\ r_z \end{bmatrix} = \frac{1}{|J|}\begin{bmatrix} zy_s - yz_s \\ xz_s - zx_s \\ yx_s - xy_s \end{bmatrix}, \quad \begin{bmatrix} s_x \\ s_y \\ s_z \end{bmatrix} = \frac{1}{|J|}\begin{bmatrix} yz_r - zy_r \\ zx_r - xz_r \\ xy_r - yx_r \end{bmatrix} \tag{19}$$

where the derivatives of the physical coordinates in Eq. (19) are computed using Eq (18) and the gradient of the basis functions. The Jacobian determinant $|J|$ is derived as:

$$|J| = \frac{\partial \mathbf{x}}{\partial t} \cdot \left[\frac{\partial \mathbf{x}}{\partial r} \times \frac{\partial \mathbf{x}}{\partial s}\right] \tag{20}$$

Having found the transformation mapping Ψ and its corresponding metrics, the interpolating polynomial ℓ_i and all the integration and differentiation operators can be built on the reference element I.

3.2.2. Building multidimensional Lagrange polynomials

The local polynomial approximation of the solution $q(\mathbf{r})$ in the reference coordinate can be expressed both in terms of basis functions $\psi(r)$ and multidimensional Lagrange polynomials $\ell(\mathbf{r})$ such that:

$$q(\mathbf{r}) = \sum_{n=1}^{N_p} \hat{q}_n \psi(\mathbf{r}) = \sum_{i=1}^{N_p} q(\mathbf{r}_i)\ell_i(\mathbf{r})$$

where $\hat{q}_n$ is the expansion modal coefficient for the nth basis function and $q(\mathbf{r}_i)$ is the conserved variable evaluated at node r_i.

The Vandermonde matrix $\mathcal{V}$ bridges between the expansion coefficients $\hat{q}$ and the grid nodal values q_i as (Hesthaven and Warburton, 2008):

$$\mathcal{V}\hat{\mathbf{q}} = \mathbf{q}, \qquad \mathcal{V}_{ij} = \psi_j(\mathbf{r}_i) \tag{21}$$

where $\mathbf{q}$ is a vector of conserved variables (ϕ or $\phi\mathbf{u}$) for all N_p grid points inside an element.

The generalized Vandermonde matrix $\mathcal{V}$ plays a pivotal role in the DG implementation and in order to preserve its stable behavior, proper selection of (1) an orthonormal polynomial basis function and (2) interpolating points on I are required (Hesthaven and Warburton, 2008).

In the current DG implementation, we have used the following basis function:

$$\psi_m(\mathbf{r}) = \sqrt{2}P_i(a)P_j^{(2i+1,0)}(b)(1-b)^i, \tag{22}$$

where $P_n^{\alpha,\beta}$ is the nth order Jacobi polynomial and

$$a = 2\frac{1+r}{1-s}, \qquad b = s$$

We have selected an interpolating nodal set similar to the Legendre–Gauss–Lobatto (LGL) nodes which are blended and warped with equidistant nodes in order to provide a well-behaved interpolation. Details of the implementation and computation of the basis function as well as the nodal set can be found in Hesthaven and Warburton (2008).

Interpolating the solution from the main LGL-type nodes to another nodal set, say cubature nodes r_i^c, requires identifying an interpolating matrix, $\mathcal{I}$, which is built once the modal coefficients of the LGL-type nodes are determined from Eq. (21) as $\hat{\mathbf{q}} = \mathcal{V}^{-1}\mathbf{q}^{lgl}$. By reapplying Eq. (21) for cubature nodes (where $\mathcal{V}_{ij}^c = \psi_j(r_i^c)$), one can write:

$$\underbrace{\mathcal{V}^c\mathcal{V}^{-1}}_{\mathcal{I}}\mathbf{q}^{lgl} = \mathbf{q}^c$$

So for any nodal sets, upon constructing proper $\mathcal{V}^{pnt}$ (in the above example $\mathcal{V}^{pnt} = \mathcal{V}^c$) the local interpolating matrix can be written as:

$$\mathcal{I} = \mathcal{V}^{pnt}\mathcal{V}^{-1} \tag{23}$$

3.2.3. Normal and tangential vectors

On every edge of an element, the normal and tangent vectors are required for construction of the numerical flux and imposing boundary conditions. Fig. 2 includes the normal $\vec{\eta}_n$ and tangent vectors $\vec{\eta}_t$ in the physical triangles. For every element, the counterclockwise orientation of (v_1, v_2, v_3) is assured which means these nodes are mapped into the respective points in the (r,s,t) coordinate. Therefore $\vec{\eta}_n$ and $\vec{\eta}_t$ on each physical edge relate directly to the similar edge in I. In other words we can write:

$$\begin{aligned} &\text{Edge1}: \quad \vec{\eta}_t = \frac{\partial \mathbf{x}}{\partial r} \\ &\text{Edge2}: \quad \vec{\eta}_t = -\frac{\partial \mathbf{x}}{\partial r} + \frac{\partial \mathbf{x}}{\partial s} \\ &\text{Edge3}: \quad \vec{\eta}_t = -\frac{\partial \mathbf{x}}{\partial s} \end{aligned} \tag{24}$$

For all the edges the normal vector can be simply computed by taking the cross product of the tangent vector and the position vector of the edge nodes $\mathbf{x}_f$:

$$\vec{\eta}_n = \mathbf{x}_f \times \vec{\eta}_t \tag{25}$$

3.2.4. Numerical integration

Computing the right-hand side of Eq. (15) at every stage of the explicit Runge–Kutta method, requires integrating the flux and source terms on an element surface (surface integrals $\int_{D_k}$) and numerical flux on its edges (edge integral $\int_{\partial D_k}$). We have employed a cubature rule to approximate the surface integrals and a similar Gaussian quadrature rule for the edge integrals.

The *surface integral* of any nonlinear functions f_h and g_h can be approximated as:

$$\int_{D_k} f_h(\mathbf{x}) g_h(\mathbf{x}) d\mathbf{x} = \sum_{i=1}^{N_c} |J_i^{c,k}| w_i^c f_h(\mathbf{x}_i^c) g_h(\mathbf{x}_i^c) \tag{26}$$

Here the N_c high order cubature nodes, $\mathbf{r}_i^c$, as well as their associated weights, w_i^c, are taken from Cools, 1999 where these are computed up to order 28 in the reference triangle I. The cubature rule includes $|J_i^{c,k}|$ as a multiplicative factor, incurred due to mapping $\mathbf{r}_i^c$ from I onto D_k.

The number of cubature points N_c varies irregularly based on the order of cubature approximation M which in return is determined as $M = 3(N+1)$ in order to yield an exact integration (Hesthaven and Warburton, 2008).

Similar to Eq. (26), the *edge integral* of any nonlinear function f_h and g_h can be approximated as:

$$\int_{\partial D_k} f_h(\mathbf{x}) g_h(\mathbf{x}) d\mathbf{x} = \sum_{i=1}^{N_g} |J_i^{g,k}| w_i^g f_h(\mathbf{x}_i^g) g_h(\mathbf{x}_i^g) \tag{27}$$

where a set of N_g Gaussian quadrature nodes, $\mathbf{r}_i^g$ and their respective weights w_i^g are constructed in I and mapped onto D_k based on Eqs. (19) and (20). In the current implementation, we have chosen $N^g = 2(N+1)$ Gaussian points on each single edge where N indicates the DG-order.

In fact since all the edge computations, including boundary condition enforcement, are performed on these Gaussian quadrature nodes, the tangent and normal vectors are constructed using these nodes based on Eqs. (24) and (25) respectively. Fig. 3 illustrates the cubature and Gaussian nodes for $N = 4$ on a single element along with the common N_p computational nodes. Note that both f_h and g_h in Eqs. (26) and (27) are interpolated onto cubature and Gaussian nodes respectively based on Eq. (23).

3.2.5. Boundary condition

When the coastal boundaries are added to the icosahedral geodesic grid, in the current shallow water solver, we only need to enforce the lateral no-flux boundary condition at the boundary edges as:

$$\vec{u} \cdot \vec{\eta}_n = 0 \tag{28}$$

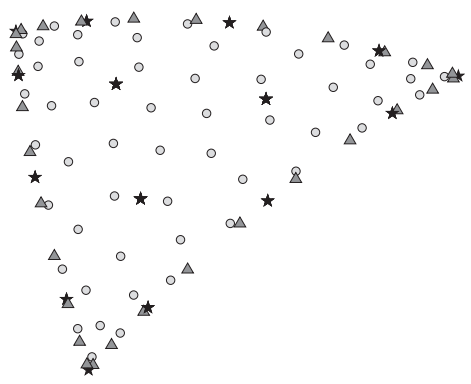

Fig. 3. Illustration of the cubature (circles) and Gaussian quadrature nodes (triangles) for $N = 4$ which results in $N^c = 18$ and $N^g = 10$ as well as $Np = 10$ computational points (stars).

For implementation purposes, the positive trace of the normal velocity u_n^+ along the boundary edge should only be corrected such that $u_n^+ = -u_n^-$.

3.3. Temporal discretization

As one of the strengths of the DG formulation relies on high-order spatial accuracy, marching in time with a low-order scheme such as the forward Euler method is not satisfactory. So in the current model we have implemented an explicit third-order Strong Stability Preserving Runge–Kutta method (SSPRK) (Gottlieb and Shu, 1998). From t^n to t^{n+1}, the solution is advanced in three stages as follows:

$$\begin{aligned} Q_1 &= Q^n + \Delta t \mathrm{RHS}(t^n) \\ Q_2 &= \frac{1}{4}\left[3Q^n + Q_1 + \Delta t \mathrm{RHS}(t^n)\right] \\ Q^{n+1} &= \frac{1}{3}\left[Q^n + 2Q_2 + 2\Delta t \mathrm{RHS}(t^n)\right] \end{aligned} \tag{29}$$

In which a variable Δt based on the CFL criterion is computed as (Hesthaven and Warburton, 2008):

$$\Delta t = \frac{2}{(N+1)^2}\left[\frac{\min(\Delta x)}{\max\left(\sqrt{u^2+v^2+w^2}+\sqrt{\phi}\right)}\right] \tag{30}$$

where the factor $(N+1)^2$ is associated with the CFL number which scales with the DG-order, in order to preserve stability of the spatial discretization even with discontinuous solutions (Gottlieb et al., 2011).

3.4. Mesh generation

Our grid generation algorithm is based on the previous work of Stuhne and Peltier (1999), Stuhne and Peltier (2006) and is briefly explained here. We also discuss the necessary transition from flat to curvilinear triangles.

3.4.1. Icosahedral grid

Mesh generation is performed within a C++ based software framework that combines interactive and script-based tools to facilitate the processing of complex geometry and data sets. The mesh generator implements a spherical version of the quadtree technique (Thompson et al., 1999), which recursively subdivides triangles in regions of interest before invoking balancing techniques to regularize the resulting grids (i.e., to ensure that triangles sharing a face also share exactly two vertices). Starting from the basic spherical icosahedron, spherical triangles are selected for subdivision based on data or interactive inputs. Selective refinement at shorelines is based on computed intersections with the Global Self-consistent, Hierarchical, High-resolution Shoreline Database (GSHHS) (Wessel and Smith, 1996), which offers polygonal data at a number of standard resolutions. Unbalanced meshes are propagated away from the coasts through the iterative subdivision of triangles that are adjacent to unbalanced triangles, and the mesh is balanced after a selected number of iterations. This technique naturally steps resolution between the coarsest and finest mesh regions.

Topographic data is projected onto completed meshes with a technique that scans through the regular grid cells of the standard ETOPO2 data set (Smith and Sandwell, 1997), finds containing mesh triangles with efficient geometric tree search methods, and thereby computes a cumulative average over each cell. This technique has advantages over naive reverse projection because it automatically averages over all data available for each grid cell without requiring large orographic databases to be loaded into

memory in their entirety. It is, moreover, straightforward to add data from supplementary databases describing particular locales.

3.4.2. Flat to curvilinear triangles

The above package tiles the surface of the sphere with *flat* triangles. However, as will be shown in Section 4.2, the use of *curvilinear* triangles is imperative in order to demonstrate fast convergence rates and more accurate results, especially for a methodology like DG where a great emphasis is placed on accuracy.

Following the early work of Sadourny et al. (1968), constructing a curvilinear triangle with order N_s requires successive splitting of every edge of an icosahedron into N_s equal arcs. For example on a triangle ΔABC, the Cartesian coordinates of point i on edge AB can be expressed as:

$$x_A x_i + y_A y_i + z_A z_i = \alpha_i$$
$$x_B x_i + y_B y_i + z_B z_i = \alpha_i'$$
$$\begin{vmatrix} x_i & y_i & z_i \\ x_A & y_A & z_A \\ x_B & y_B & z_B \end{vmatrix} = 0$$

where $\alpha_i = \cos(iN_s/\widehat{AB})$, $\alpha_i' = \widehat{AB} - \alpha_i$ and $\widehat{AB}$ denotes arc length AB in radians. To close the above system of equations, points A, B and i must be coplanar which is enforced by the third equation above. All the grid points are determined following the same approach. Once these equidistant grid points are in place for order $N_s > N$, they are redistributed to LGL-type nodes. We set $N_s = N + 2$, where N is the polynomial order for the DG scheme to ensure less error due to geometrical approximation of the spherical surface than the numerical errors (see Section 4.2 for more information). Fig. 4 illustrates the icosahedral geodesic grids before and after refining the flat triangles into curvilinear triangles with $N_s = 4$.

As a consequence of using curvilinear triangles, the transformation metrics and thus $|J|$ in Eq (20) would not be constant any longer on an element. So in all the integrations including the transient term in Eq (15), because of the mapping from $\mathtt{I}$ to $\mathtt{D}$, $|J|$ must remain inside the integral and be treated accordingly.

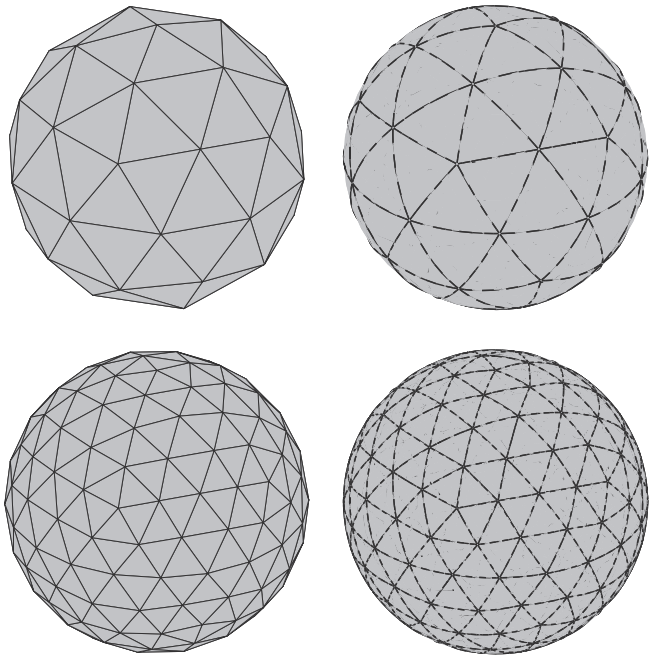

Fig. 4. Illustration of a series of icosahedral grids with varying number of triangular elements before and after grid refinement using $N_s = 4$.

3.5. MPI parallelization

The explicit DG formulation, despite benefiting from its unique conservation properties and high orders of accuracy, is obliged to follow the CFL criterion as explained in Section 3.3 and hence small time steps are imposed (Nair et al., 2005; Nair et al., 2005; Giraldo, 2006; Laeuter et al., 2008).

In ocean and atmospheric modeling, long simulation times are inevitably required. For the purposes of the current work, the transient time to reach equilibrium in tidal simulations can extend to as many as 20–40 model days. In addition, it is desirable to take advantage of the unstructured grid framework and refine the mesh to for example 3–6 km resolution in regions of interest which in turn leads to $\Delta t \approx 1$–2 s for stability reasons. For such a resolution the model time step (3-stages of Runge–Kutta) can take roughly 20–30 s when compiled efficiently in FORTRAN and run sequentially, assuming no memory issues arise. That means the total computational time for one single tidal simulation could extend to 1–2 years! These estimates are based on one of the tidal simulations presented in the results section of paper, in which the grid resolution varies from about 120 km in the deep ocean to about 15 km on all global coastlines ($K = 557,657$ elements). With $np = 512$ computing cores employed, on the contrary, the elapsed wall clock time for the M_2 tide simulation was reduced to 3 days to obtain 21 model days of data, employing an $N = 3$ order DG methodology.

Furthermore the DG scheme, in contrast to finite volume and finite element methods, is characterized by almost perfect scaling due to its compact stencil and small communication halo (Kelly and Giraldo, 2012). So the aforementioned restriction on time stepping can be alleviated provided that we take advantage of this scaling property and efficiently parallelize the model. We have parallelized the current shallow water solver using a pure Message Passing Interface (MPI) methodology as discussed below.

3.5.1. Domain decomposition

The computational domain is decomposed into np partitions using the well-known and widely used package METIS (Karypis and Kumar, 1998). The output of this decomposition is a vector list of elements along with their respective processor *rank* to which they belong. Fig. 5 illustrates an example of such a decomposition where each color indicates one computational domain which is handled by a single core.

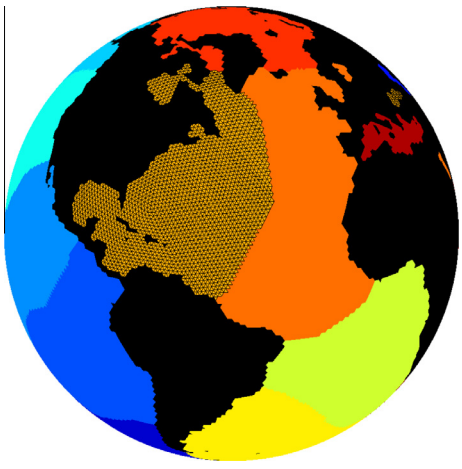

Fig. 5. Illustration of the domain decomposition using METIS (Karypis and Kumar, 1998) package where every color indicates one domain which belongs to one computational core.

Table 1
The pseudo code for the MPI parallelized Shallow Water code.

Pseudo code: RHS Computation
– `Interpolate the solution into Gaussian and cubatur nodes`
– `Find the positive and negative trace of the conserved variables`
– `Impose the no-flux boundary condition if needed`
– `Boundary exchange: Non-blocking message sending and receiving`
– `Compute all the surface integrals for internal elements`
– `Waitall`
– `Read the received message`
– `Compute the numerical flux`
– `Compute the RHS`

3.5.2. Message passing

When the MPI code is initialized, identical copies of the code are available for all the requested cores. What differs between cores from an algorithmic standpoint are some local information such as how many elements K_{loc} exist in each domain and some global-to-local information such as connectivities between global elements which identifies the surrounding neighbors. There is no need for access to a shared memory since all the above required information is computed independently for each processor depending on its *rank* and the domain decomposition outputs.

For the *internal* elements of each domain, the assigned core computes all the surface and edge integrals of Eq. (15) independently, as if the code was running sequentially (i.e., without having to share any information with other cores). However for the *boundary* elements, the computation of the numerical flux as described in Eq. (17) requires the positive trace of the information which lies in the neighboring domain (or core). This is the point where the communication between cores comes into play. Even for the boundary elements, the surface integral of Eq. (15) requires no exterior information and is entirely local to the domain.

We have employed a non-blocking send and receive technique (`MPI_ISEND` and `MPI_IRECEIVE`) which hides the communication latency while the messages are on the fly. In other words (as shown in the form of the pseudo code in Table 1) the boundary exchange is initiated at the beginning of RHS computation and rather than waiting for the messages to be sent/received right away, the rest of the locally *internal* computations are performed while the communication is being done. The positive trace of the boundary elements is needed at the very last step before finishing the RHS computation by which time the message correspondence between cores is almost done, minimizing the waiting time.

4. Benchmark results and discussion

In this section, the parallel performance, accuracy and convergence of the proposed model are evaluated in the context of a set of aquaplanet benchmarks; namely cases 2 and 5 from the standard test suite of Williamson et al. (1992) and the development of a barotropically unstable jet due to an initial perturbation of a balanced flow as proposed by Galewsky et al. (2004).

4.1. Scaling

The parallel performance of the model is studied here by performing a strong scaling test where the size of the problem is kept constant but the number of computation cores are successively increased. An icosahedral grid with $K = 327,680$ elements (i.e., grid spacing of about 50 km) and DG-order $N = 3$ is chosen. The initial conditions are based on case 5 in (Williamson et al., 1992) and the wall-clock times are reported after 1 day of model run for convenience.

Fig. 6 demonstrates the results of the scaling analysis. The left plot shows the variations of the wall-clock time for increasing number of processors (np) on a log–log scale. The wall-clock time is almost precisely halved upon doubling of np which is excellent and indicates almost perfect scaling. The same conclusion is evident from the rightmost plot that shows the speedup variation with np. It was not feasible to run the code at this resolution sequentially, so for speedup calculations, the wall-clock time for $np = 1$ is assumed to be eight times more than the elapsed time for $np = 8$.

The DG formulation as described in Eq. (14), is characterized by a very compact communication stencil which only requires the information on the three edges of the element as well as on the common edge from the immediate neighbors (Cockburn and Shu, 1998). The above spectacular linear scaling is achieved mainly due to this localized formulation which contrasts with the continuous Galerkin formulation as also established by Kelly and Giraldo (2012).

4.2. Convergence study

The DG formulation provides the added flexibility of delivering a converged solution solely by increasing polynomial orders (p-refinement). Here we investigate the convergence properties of the proposed model by performing both h and p-refinement tests.

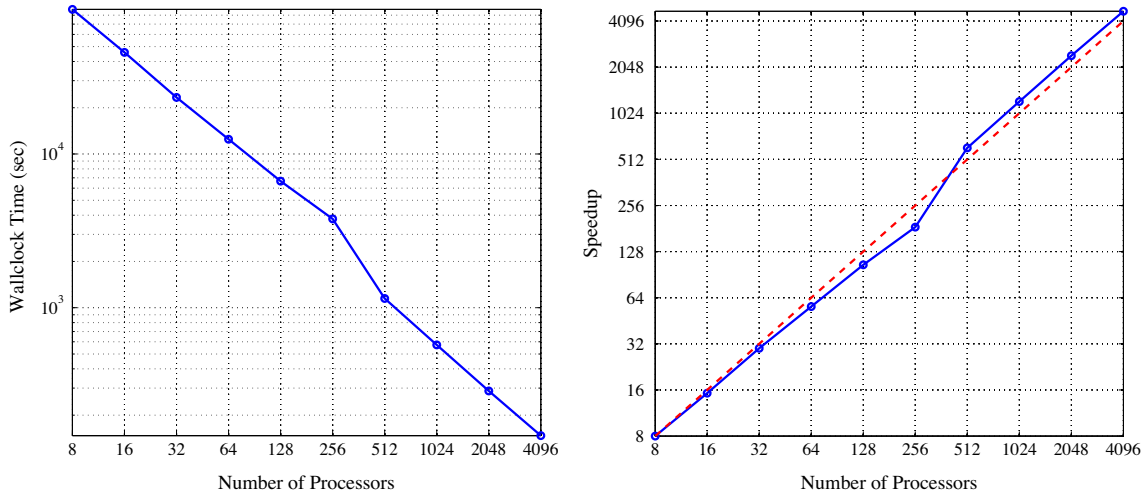

Fig. 6. Strong scaling performance of the MPI shallow water DG code.

The model is initialized by a zonal wind field (solid body rotation) and a geostrophically balanced height field as per test case 2 of Williamson et al. (1992) with:

$$\omega = \frac{2\pi}{12\ \text{days}}, \quad \mathbf{u} = [-\omega y, \omega x, 0]^T$$

$$\phi = \phi_0 - \left(a\omega u_0 + \frac{u_0^2}{2}\right)(\sin\theta\cos\alpha - \cos\lambda\cos\theta\sin\alpha)^2$$

where $u_0 = a\omega$ and the initial geopotential height is $\phi_0 = 2.94 \times 10^4\ \text{m}^2/\text{s}^2$. The present results are only for $\alpha = 0$ after 5 model days. Also since the problem is steady, the final solution is essentially identical to the initial flow fields. Taking the reference exact solution as q, the diagnostic L_2 error norm for the discretized numerical solution, q_h is calculated as follows:

$$L_2(q) = \left\{\frac{\int_S [q(\mathrm{x}) - q_h(\mathrm{x})]^2 dS}{\int_S q(\mathrm{x})^2 ds}\right\}^{\frac{1}{2}}$$

$$L_2(\mathrm{q}) = \left\{\frac{\int_S \sum_{i=1}^{3}\left[q^{(i)}(\mathrm{x}) - q_h^{(i)}(\mathrm{x})\right]^2 dS}{\int_S \|q(\mathrm{x})\|^2 ds}\right\}^{\frac{1}{2}}$$

where $\int_S$ is an integration over the whole surface of the sphere. The first expression above is used for the scalar height field and the second for the wind field.

Fig. 7 shows a log–log variation of the L_2-norm with $K^{1/2}$ (as a measure of grid spacing) for the velocity and height fields with flat and curvilinear triangles. The mean rate of convergence for each polynomial order N is also shown in this figure. As will be inferred from the top two panels of this figure, when the sphere is tiled with flat triangles, not only is the optimal convergence rate of $N + 1$ not observed, but also increasing the order of accuracy has no impact whatsoever on the accuracy of the results. This problem arises due to the fact that geometrical errors have become the most prominent numerical errors. In other words, poor approximation of the sphere (see Fig. 4) eliminates p-convergence. In the bottom two plots of Fig. 7, curvilinear tessellations of the sphere have been exploited which clearly improves the convergence rate to its optimal value.

For a plain icosahedron ($K = 20$ elements) in Fig. 7, the L_2-error norm can quickly reach about 10^{-5} with a higher order DG method of $N = 8$. The equivalent accuracy in terms of L_2-error can be obtained on a grid with 2^{10} times more elements ($K = 20,480$ elements) and a second order scheme ($N = 2$). In terms of the sequential wall-clock time, the former took about 40 s while the latter run continued for about 3 h! This superior performance of a higher-order DG method, is mainly applicable to atmospheric studies in which no lateral boundaries are present provided that the computed fields are sufficiently smooth; for oceanic applications the intricacy of the coastal configuration inherently requires use of a finely resolved mesh. However the deep ocean still benefits from this capability, especially if N increases from shallow to deep areas while the mesh becomes less refined.

4.3. Isolated mountain induced Rossby waves

This is test case 5 in (Williamson et al., 1992) in which a zonal flow impinges on a single broad mountain so that the dominant form of the response consists of a train of Rossby waves. There is no analytical solution for this test case, but comparisons are made with a high-resolution reference solution provided by the German Weather Service from a T426 spectral simulation (31 km resolution at the equator) using the shallow-water spectral model of the National Center for Atmospheric Research (NCAR) (Jakobchien et al., 1995).

The initial conditions for both height and wind field are as in case 2 but $h_0 = 5960m$ and $u_0 = 20m/s$. The mountain topography is specified as:

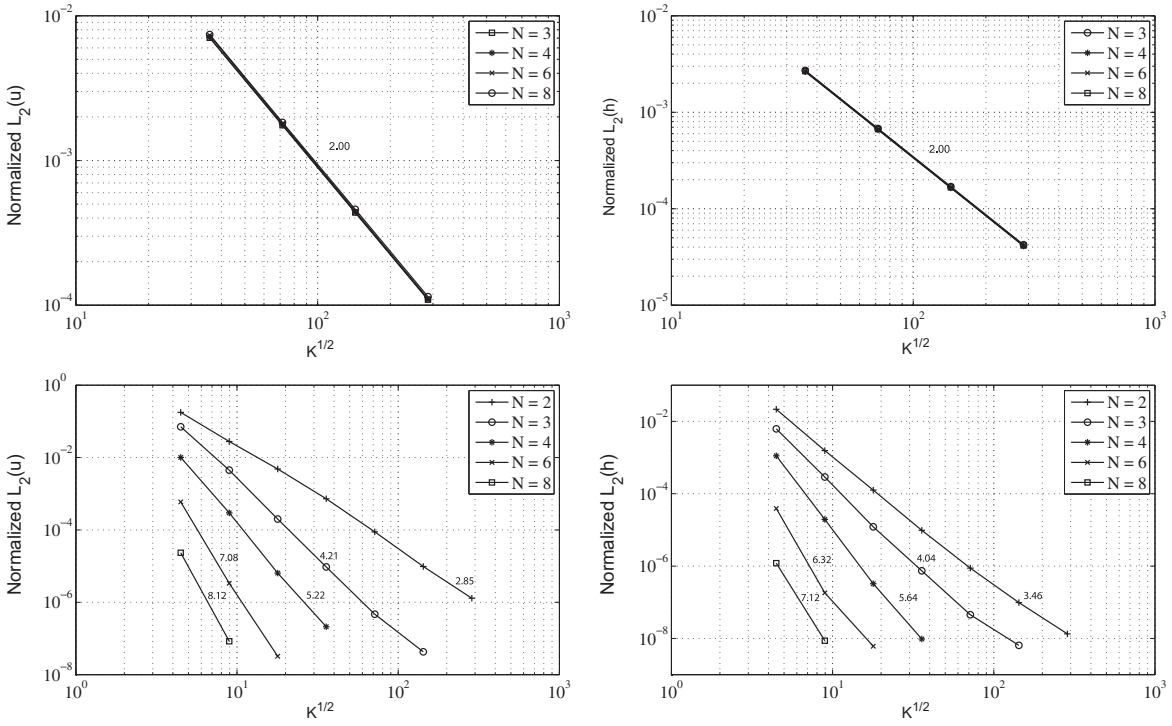

Fig. 7. Variation of L_2-norm for the velocity (left plots) and height fields (right plots) where the spherical surface is tiled with flat triangle (top plots) and curvilinear triangles (bottom plots).

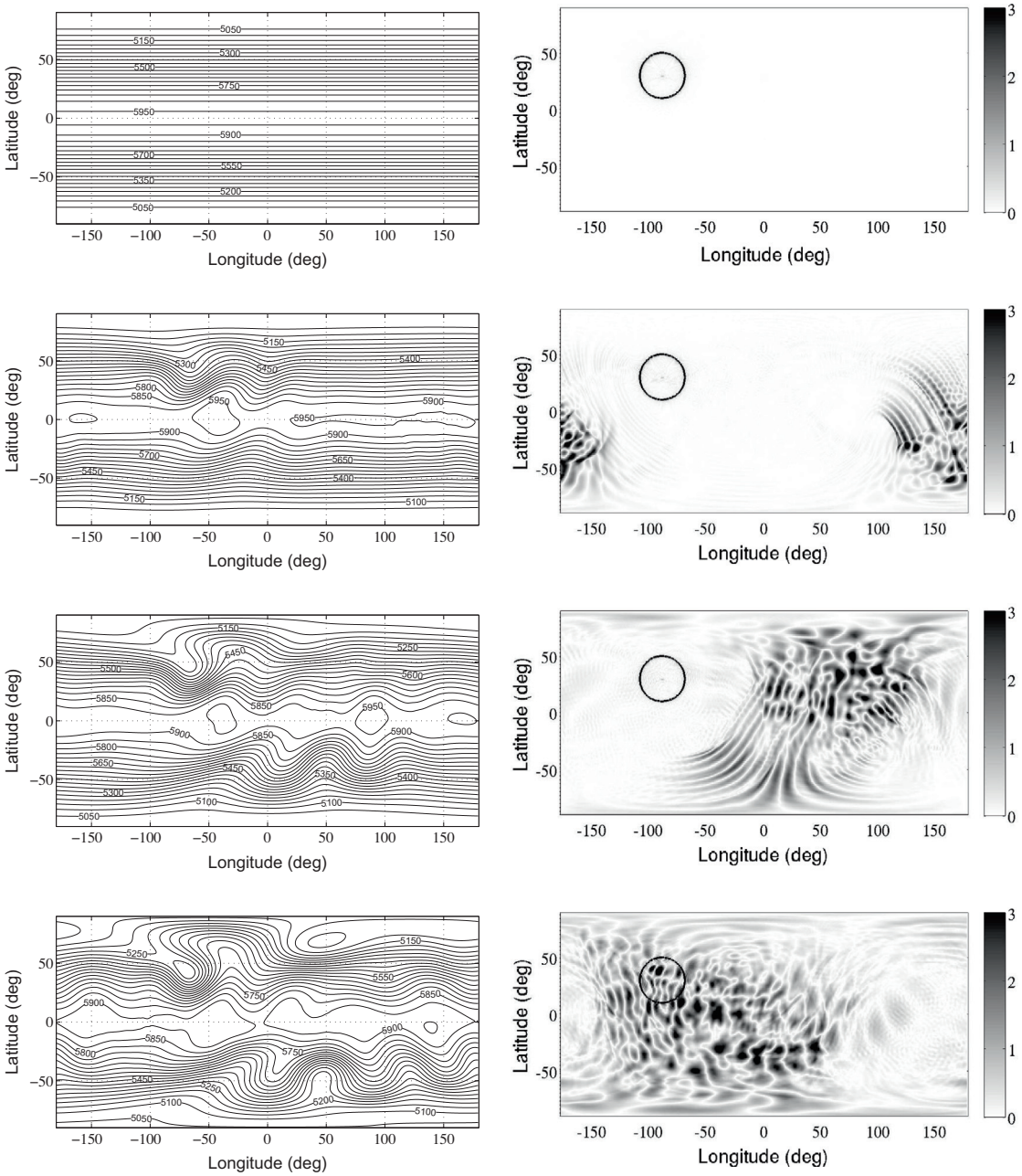

Fig. 8. Model results for test case 5 of Williamson et al. (1992) with $N = 3$ and level 7 grid. Left: Total height field at day 0, 5, 10 and 15 of zonal flow over an isolated mountain. The contour interval is 50 from 5050 to 5950. Right: Comparison with high-resolution reference results from German Weather Service. Absolute difference in the height field $\|h - h_{\text{ref}}\|$ is plotted for the same days.

$$h_s = h_{s0}(1 - r/R)$$

where $h_{s0} = 2000$ m, $R = \pi/6$ and $r^2 = \min[R^2, (\lambda - \lambda_c)^2 + (\theta - \theta_c)^2]$ with $\lambda_c = 3\pi/2$ and $\theta_c = \pi/6$.

Fig. 8 illustrates contour plots of the total height field h at 5-day intervals as well as the absolute "error" contours when compared against the reference solution. The pattern of the difference contours is almost identical to the similar results reported in (Blaise and St-Cyr, 2012) which were based upon application of a cubed sphere DG model. These residual plots might represent the phase differences in the surface gravity wave component of the response to the topographic forcing and thus might be better described as representing the difference in the generated surface gravity waves between different models.

4.4. Barotropic instability of a balanced zonal jet

In this test case, a mid-latitude zonal jet with a high meridional gradient is prescribed as the initial wind field so that the initial state satisfies the condition for linear barotropic instability (e.g., see Vallis, 2006). The initial height field is also determined by numerically integrating the balance equation while maintaining a fixed global mean layer depth. A localized Gaussian bump, centered at the jet core and vanishing at the pole, is added to the height field as an initial perturbation which induces the development of barotropic instability (please refer to (Galewsky et al., 2004) for the exact form of initial conditions). The inviscid variant of this test case is investigated in this section.

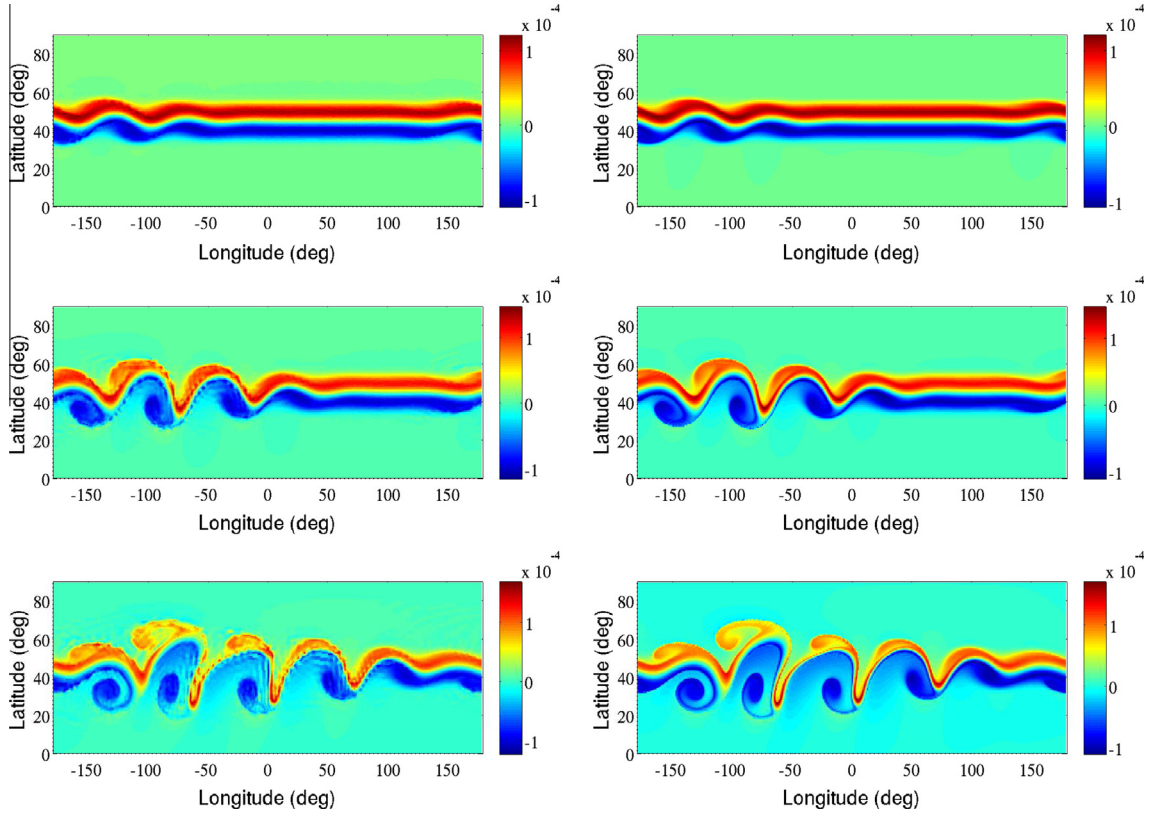

Fig. 9. Development of barotropic instability from perturbing a geosptrophically balance jet field. The vorticity contours resulted from the current DG model with $N = 3$ on level 5 (left plots) and level 7 grid (right plots) after 4, 5 and 6 days (from top to bottom).

This is a challenging test case because of its high degree of nonlinearity and the sharp gradients that develop within the zonal jet. In addition, a common difficulty arises due to the misalignment of icosahedral grids with the prescribed zonal jet that results in a wavenumber five disturbance pattern in the flow field even with zero perturbation (St-Cyr et al., 2008; Laeuter et al., 2008; Ii et al., 2010). Nonetheless, in a geostrophically balanced flow, the unperturbed zonal jet must remain unchanged while the numerical solution is evolving and this is usually achieved by increasing the spatial resolution. In our DG model and in the absence of perturbation, the same disturbance pattern is observed for a very coarse resolution of the level 4 icosahedral grid (about 4° resolution with $K = 5120$) but not in a level 5 grid (about 2° resolution with $K = 20,480$) both with $N = 3$.

Since there is no available reference solution, here we compare the results on a level 5 grid with the results obtained for the same problem on a higher resolution level 7 grid (almost 0.5° resolution with $K = 327,680$) while keeping $N = 3$ in both cases. The vorticity fields after 4, 5 and 6 days of evolution are shown in Fig. 9 illustrating the development of the barotropic instability. As inferred from this figure, although the small-scale features are captured more accurately in the more refined grid, the general structure of the flow fields is similar and resembles qualitatively and quantitatively the patterns reported in (Galewsky et al., 2004; St-Cyr et al., 2008; Ii et al., 2010).

5. Tidal simulations

For this primary target problem, the governing equations are extended to include the influence of both boundary layer drag as well as the internal tide drag in the deep ocean together with the influence of gravitational self-attraction and loading as described in Section 2.2. Here, we will focus entirely upon the dominant semi-diurnal M_2 tide with amplitude and frequency of $A = 24.2334 \times 10^{-2}$ m, and $\omega = 1.405189 \times 10^{-4}$ s^{-1} respectively with a Load Love number of $\kappa = 0.693$ (Arbic et al., 2004 Table 1) employed as basis for the approximation of the influence of gravitational self-attraction and loading. In our model, the solution for this dominant tidal constituent usually reaches equilibrium after about 12 days of simulated time. The M_2 tidal amplitude (A) and phase (ψ) have been computed by fitting a cosine function $A\cos(\omega t - \psi)$ to the model results using a nonlinear least square method.

In order to validate our numerical results, we compare them with solutions from TPXO 7.2, an updated version of the global inverse model by Egbert et al. (1994), which is constrained by the TOPEX/Poseidon (T/P) satellite altimeter data. Fig. 10 depicts global graphics of the M_2 tidal amplitude and phase for both the DG model and TPXO 7.2 altimetry based results. The numerical results from the DG model will be seen, on the basis of visual inspection, to agree very well with the assimilated solutions in both amplitude and phase. In particular, the regions of high and low tidal elevation match well and the amphidromes (where the phase contour lines meet) are located in almost the identical positions. However we do observe more locally energetic tides in the DG-model especially near certain coastlines. Care must be taken in interpreting the inverse model results because the T/P datasets are only available equatorward of 66° and are most reliable (with an accuracy of a few centimeters) in the deep ocean where $h > 1000$ m (Egbert et al., 2004).

The time averaged discrepancy between the altimetry based observation and model prediction can be diagnosed as an area averaged deviation from the reference solution and is calculated as:

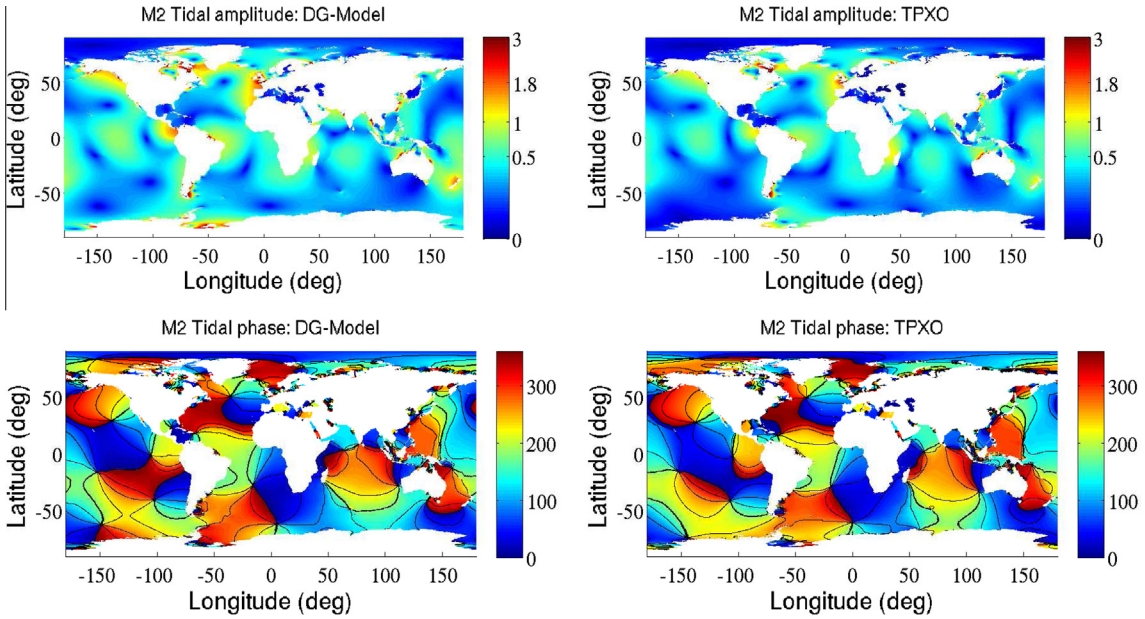

Fig. 10. The global picture of the M_2 tidal amplitude (top) and phase (bottom) from Left: DG-model with $N = 3$ and Right: TPXO 7.2 dataset on a a grid with about 60 km resolution in deep ocean and 7.5 km around the global coasts.

$$\overline{\Delta\zeta} = \left\{ \frac{\langle \iint (\zeta - \zeta_{tpx})^2 dA \rangle}{\iint dA} \right\}^{1/2}$$

where brackets refer to time-averaging over one tidal period. Also in order to evaluate the fraction of the sea surface height variance captured by our DG model, $\delta = 1 - (\overline{\Delta\zeta}/\overline{\zeta}_{tpx})^2$, a temporally and spatially averaged reference signal $\overline{\zeta}_{tpx}$, is computed as:

$$\overline{\zeta}_{tpx} = \left\{ \frac{\langle \iint \zeta_{tpx}^2 dA \rangle}{\iint dA} \right\}^{1/2}$$

For an M_2 tidal simulation with a resolution varying from a level 7 to 10 quadtree mesh (coarse resolution of 60 km in the deep ocean increasing to about 7.5 km near coastlines globally) and DG-order $N = 3$, the above diagnostics are calculated after excluding high-latitude and shallow tides (as is traditional). This yields $\overline{\Delta\zeta} = 12.6$ cm and from the TPXO 7.2 solution $\overline{\zeta}_{tpx} = 25.9$ cm which results in $\delta = 76.3\%$. This variance fraction improves to $\delta = 90.5\%$ (with $\overline{\Delta\zeta} = 11.6$ cm and $\overline{\zeta}_{tpx} = 37.5$ cm) when computing for tidal amplitude only and ignoring errors in phase. In fact, the relatively larger errors in tidal phase are a consequence of the crude scalar estimation of the self-attraction and loading term as pointed out by Ray (1998). However, according to our results the tidal amplitude is not affected severely by this approximation.

A closeup illustration of the multiple levels of grid refinement is given in Fig. 11 where the coloring shows the predicted M_2 amplitude.

The model can also be assessed from an energetics standpoint. The kinetic and potential energies are calculated as:

$$\begin{aligned} KE &= \tfrac{1}{2}\rho_0 \iint h\mathrm{u}\cdot\mathrm{u}\, dA, \\ PE &= \tfrac{1}{2}\rho_0 g \iint \zeta^2 dA \end{aligned} \tag{31}$$

where ρ_0 is the density of ocean water. At equilibrium, the total tidal energy of the system shows no secular variation. The dissipation terms are $\mathcal{D}_{dis} = \mathrm{D}\cdot\mathrm{u}$ where $\mathrm{D} = \mathrm{D}_{\mathrm{BL}} + \mathrm{D}_{\mathrm{IT}}$ (as described in Section 2.2) for the boundary layer and internal tide partitioning of the energy dissipation respectively.

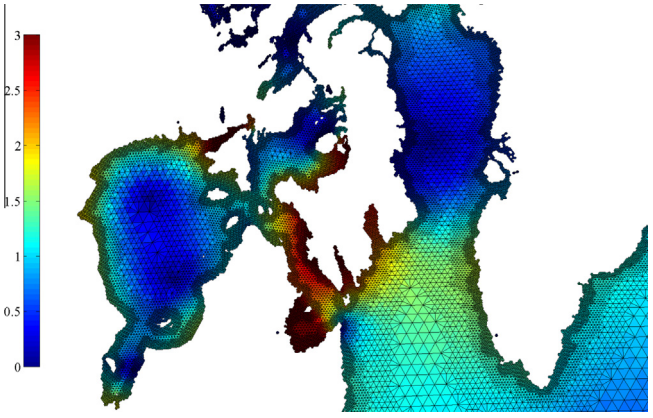

Fig. 11. The regional picture of the M_2 tidal amplitude around Hudson Bay using the DG model with $N = 3$ and a global grid with about 60 km resolution in deep ocean and 7.5 km around the global coasts.

For the purpose of analysing the energetics of the tidal solution we have employed both uniform grids and coastally refined grids. The uniform grids to be employed are the following:

- *U1*: Global level 6 quadtree mesh ($\Delta x \approx 120$ km, $K = 57,482$)
- *U2*: Global level 8 quadtree mesh ($\Delta x \approx 30$ km, $K = 928,450$)

To compare with the results obtained for the uniform grids our nonuniform grid configurations have been built with successive levels of refinement from the deep ocean towards global shorelines as explained in Section 3.4.1. These nonuniform grids are the following:

- *NU1*: Global coastal refinement up to level 7 quadtree mesh ($\Delta x \approx 60$ km) and level 5 ($\Delta x \approx 240$ km) in the deep ocean ($K = 101,043$).
- *NU2*: Global coastal refinement up to level 9 quadtree mesh ($\Delta x \approx 15$ km) and level 5 ($\Delta x \approx 240$ km) in the deep ocean ($K = 508,647$).

- *NU3*: Global coastal refinement up to level 9 quadtree mesh ($\Delta x \approx 15$ km) and level 6 ($\Delta x \approx 120$ km) in the deep ocean ($K = 557,657$).
- *NU4*: Global coastal refinement up to level 10 quadtree mesh ($\Delta x \approx 7.5$ km) and level 7 ($\Delta x \approx 60$ km) in the deep ocean ($K = 1,368,127$).

These grid configurations have been chosen so as to illustrate the effect of grid refinements on the tidal energetics and its global dissipation. To our knowledge such a comparison is unprecedented, primarily because no adequate numerical framework, such as is embodied in the current DG methodology, has been available.

Tables 2 and 3 summarize the model results for global energy and dissipation terms respectively with the above grid configurations. They also include the partitioning of the global kinetic and potential energies between deep ocean and shallow seas and between poleward and equatorward of $\theta = 66^\circ$. Furthermore, the dissipated power in terms of the boundary layer and internal tide drags are also calculated as a function of this partitioning. Wherever possible, relevant values are reported from the T/P altimeter data together with the assimilated solutions of the TPXO.5 inverse global model (Egbert and Ray, 2001; Egbert and Ray, 2003). Notice that, while the total dissipation $\mathcal{D}_{\text{tot}} \approx 2.44TW$ is rigorously inferred from T/P observations, its shallow/deep division into $\mathcal{D}_{\text{BL}}$ and $\mathcal{D}_{\text{IT}}$ results from the assimilated TPXO.5 model and so there is clearly an issue concerning their accuracy which is reflected in Table 3 by the question marks. The results tabulated in Tables 2 and 3 motivate the following observations:

- Model resolution plays an important role in the prediction of tidal energetics and dissipation, in agreement with the previous arguments of Egbert et al. (2004) Fig. 2 and Griffiths and Peltier, 2009 Fig. 5. However because of the robustness of the newly developed DG model in handling millions of nonuniform elements in parallel, we are now able to segregate the effect of grid refinements in the deep ocean as opposed to refinements in the coastal regions in the global tidal energy budget.
- In the uniform cases, the resolution of the *U1* grid is increased by a factor of 4 in *U2* and as a consequence, the relative error (ϵ) in E_{tot} reduces from 145% to 52.3% and from 54.5% to 33.2% in $\mathcal{D}_{\text{tot}}$. This is in contrast with the minimal sensitivity of PE and KE to the grid resolution in (Egbert et al., 2004 Fig. 2) (the case where their internal tide parameterization is active). As a consequence of increasing mesh resolution (either uniformly or nonuniformly), more topographic and coastal features are resolved and we believe the sensitivity of the results to grid resolution is essential and originates from the physics of the problem.
- On the *U1* grid, the effect of increasing the DG order from $N = 3$ to $N = 5$ seems to have small but not negligible impact on the accuracy of the results. It is interesting that $\mathcal{D}_{\text{BL}}$ increases (only in shallow seas) while the total available energy decreases. This may imply that nonlinearities associated with the boundary layer drag especially in shallow seas are more accurately captured in our nonlinear global tidal model. For the other grids, we have only run the model using $N = 3$ for the purpose of obtaining illustrative results.
- In the case *NU2*, the refined coastal resolution, even with a coarse grid spacing of 240 km in the deep ocean, dramatically improves the predictions for KE, PE and $\mathcal{D}_{\text{tot}}$. The error in E_{tot} becomes 18% while for $\mathcal{D}_{\text{tot}}, \epsilon = 11\%$. In the more intense case of *NU4*, however, these errors are further reduced to 15.7% and 6.6% respectively. It is interesting that in *NU3*, although the global dissipation is within 1.2% of the results inferred from

Table 2
The effect of various grid configurations on energetics of the global M_2 tides. The results from our purely numerical DG model are compared with the results inferred from T/P altimetry and the assimilated solution of TPXO.5 (Egbert and Ray, 2003 Table 1).

Global energy ($\times 10^{17} J$)	TPXO.	U1	U1, $N = 5$	U2	NU1	NU2	NU3	NU4
E_{tot}	–	10.08	9.90	6.54	8.30	4.94	5.26	4.82
PE	–	4.86	4.76	3.09	3.87	2.33	2.49	2.21
KE	–	5.22	5.14	3.45	4.43	2.60	2.77	2.61
$\lvert\theta\rvert \leqslant 66^\circ,\ h \geqslant 1000$ m								
E_{tot}	3.06	7.50	7.32	4.66	6.19	3.61	3.82	3.54
PE	1.28	3.47	3.38	2.13	2.78	1.63	1.73	1.54
KE	1.78	4.03	3.94	2.53	3.41	1.98	2.09	2.00
$\lvert\theta\rvert \leqslant 66^\circ$								
E_{tot}	–	9.56	9.37	6.14	7.94	4.69	4.98	4.57
PE	–	4.60	4.50	2.90	3.69	2.22	2.36	2.09
KE	–	4.96	4.87	3.25	4.25	2.47	2.63	2.48

Table 3
The effect of various grid configurations on the global dissipation of M_2 tides in terms of boundary layer and internal tide dissipation. The results from our purely numerical DG model are compared with the results inferred from T/P altimetry and the assimilated solution of TPXO.5 (Egbert and Ray, 2003 Table 1).

Global dissipation ($\times 10^{12} W$)	TPXO.	U1	U1, $N = 5$	U2	NU1	NU2	NU3	NU4
$\mathcal{D}_{\text{tot}}$	2.44	3.77	3.84	3.25	3.33	2.17	2.41	2.28
$\mathcal{D}_{\text{BL}}$	1.65?	3.51	3.58	2.54	2.96	1.77	1.96	1.74
$\mathcal{D}_{\text{IT}}$	0.78?	0.26	0.26	0.70	0.37	0.40	0.45	0.54
$\lvert\theta\rvert \leqslant 66^\circ,\ h \geqslant 1000$ m								
$\mathcal{D}_{\text{tot}}$	–	0.22	0.22	0.56	0.29	0.28	0.31	0.37
$\mathcal{D}_{\text{BL}}$	–	0.03	0.03	0.01	0.02	0.01	0.01	0.01
$\mathcal{D}_{\text{IT}}$	–	0.19	0.19	0.55	0.27	0.27	0.30	0.36
$\lvert\theta\rvert \leqslant 66^\circ$								
$\mathcal{D}_{\text{tot}}$	–	3.23	3.26	2.82	2.90	1.90	2.08	2.00
$\mathcal{D}_{\text{BL}}$	–	2.98	3.00	2.12	2.54	1.50	1.63	1.46
$\mathcal{D}_{\text{IT}}$	–	0.26	0.25	0.70	0.36	0.40	0.45	0.54

T/P data, E_{tot} still differs by 24.8%, suggesting once more the importance of deep ocean refinement in correctly predicting both tidal energy and its dissipated power.

- Focusing on *NU1* and *NU2*, while the resolution in the deep ocean is similar, the mesh is four times more refined in *NU2* near shorelines. This coastal refinement seems to have a huge impact on the tidal energetics and the dissipated power which is not surprising since a better realization of geometry must lead to a more accurate solution. Notice that while $\mathcal{D}_{IT}$ is almost the same in these two cases, a more accurate representation of the coastlines manifest itself only in $\mathcal{D}_{BL}$. This trend is also observed in other cases where deep water refinement enhances $\mathcal{D}_{IT}$ predictions whereas refinement of near-shorelines leads to more dissipations due to bottom boundary layer drag $\mathcal{D}_{BL}$. In fact this argument is more evident in tidal dissipation at $h \geqslant 1000$ where the main sink of energy is due to $\mathcal{D}_{IT}$, leaving $\mathcal{D}_{BL}$ to be functioning solely in shallower water.
- Nonetheless, the role of internal tide generation (as parameterized in our model) seems not to be restricted only to the deep ocean. In fact an interesting partition of about 33% (as the ratio of $\mathcal{D}_{IT}$ in shallow seas to the global dissipation) is observed in *NU2*, *NU3* and *NU4*.
- The embedded unstructured triangulation of the sphere implemented in the model, makes investigation of the high latitude and polar tides feasible. From our results in grids *NU2*, *NU3* and *NU4*, about 5% of the total available M_2 tidal energy lies at latitudes $|\theta| \geqslant 66^\circ$. This is especially important as the analyses of Griffiths and Peltier (2008); Griffiths and Peltier, 2009 have demonstrated that the tides in the polar regions, especially the Arctic Ocean, are massively amplified under Last Glacial Maximum (LGM) conditions when the Arctic Ocean basin becomes resonant at the M_2 period.

6. Summary and conclusion

In this paper, we have described the development of a higher order, parallel framework based on the discontinuous Galerkin formulation which is particularly aimed at multi-scale tidal simulations. The different numerical ingredients required in the development of this structure, including the MPI parallelization, were fully described.

We employed a strong scaling test for the purpose of analyzing the parallel performance of the model and this enabled us to demonstrate essentially perfect scaling up to 4096 cores beyond which the model has not yet been tested. In a convergence study, we demonstrated the capability of such a higher order method and emphasized the importance of employing curvilinear rather than flat triangles in order to achieve the fast convergence rates of $N+1$.

Further validations were obtained by using an unsteady standard aquaplanet test case from Williamson et al., 1992 investigating the generation of Rossby waves from the flow over an isolated mountain. We compared our results with the high resolution spectral model of the German Weather Service and found small spurious patterns in the height field analogous to those published recently by Blaise and St-Cyr (2012). These small scale patterns might be associated with a phase shift in surface gravity waves predicted by different models. In addition to this test case, a more recent and challenging test involving the development of barotropic instability of a zonal jet was used to initialize the model and the results agreed very well with other published works.

We also demonstrated the model results for global M_2 tides on a variety of nonuniform grid configurations. Tidal amplitude and phase maps compared reasonably with TPXO 7.2 solutions. The scalar approximation of the self-attraction and loading seems to affect the phase predictions only; For energetics studies, because of the time averaging over a tidal period, minor phase shifts do not affect adversely the model predictions. The tidal energetics in terms of available potential and kinetic energy were diagnosed and increasingly converged results were obtained as we refined the mesh. This is consistent with the conjectures made by Egbert et al. (2004) and Griffiths and Peltier (2008). But more interestingly, the deep ocean need not be as finely resolved as the coastal areas in order to obtain accurate estimates of total available energy as well as the total dissipated energy. No filtering or numerical limiters were necessary in our simulations while we also employed no smoothing of the bottom topography. This allowed an accurate representation of sharp gradients in the bottom topography.

Future work will involve testing the model on a larger number of computational cores and adding more refined topographic data for local tidal studies within our global model. The iterative approximation of self-attraction and loading must also be included in the model in order to better estimate the tidal time series. Using the developed model, one can study different tidal constituents not only under modern conditions but also during the Last Glacial Maximum (LGM). These analyses can be focused on different regions of interest, for example the Arctic Ocean and the southern hemisphere western Atlantic in the vicinity of the Patagonian shelf. Furthermore, global maps of dissipation from the anisotropic internal tide parameterization utilized in the current model, can be generated with a global grid that is locally resolved at regions of high topographic gradients and super-refined near shorelines; capabilities which have become available because of the efficient multi-scale properties of the current model.

Acknowledgments

Computations were performed on the GPC supercomputer at the SciNet HPC Consortium. SciNet is funded by: the Canada Foundation for Innovation under the auspices of Compute Canada; the Government of Ontario; Ontario Research Fund - Research Excellence; and the University of Toronto. The first author would like to extend his thanks to Dr. Jonathan Dursi for his kind and helpful guidance on parallelizing the code. The research of WRP and GS is funded by NSERC Grant A9627 and NWMO funding to WRP. Additional funding for this project was provided by NOAA [NAI10AR4310101].

References

Accad, Y., Pekeris, C., 1978. Solution of tidal equations for M2 and S2 tides in world oceans from a Knowledge of tidal potential alone. Philosophical Transactions of the Royal Society A-Mathematical Physical and Engineering Sciences 290, 235–266.

Aizinger, V., Dawson, C., 2002. A discontinuous Galerkin method for two-dimensional flow and transport in shallow water. Advances in Water Resources 25, 67–84.

Arbic, B., Garner, S., Hallberg, R., Simmons, H., 2004. The accuracy of surface elevations in forward global barotropic and baroclinic tide models. Deep-Sea Research Part II-Topical Studies in Oceanography 51, 3069–3101.

Bernard, P.E., Chevaugeon, N., Legat, V., Deleersnijder, E., Remacle, J.F., 2007. High-order h-adaptive discontinuous Galerkin methods for ocean modelling. Ocean Dynamics 57, 109–121.

Bernard, P.E., Remacle, J.F., Legat, V., 2009. Boundary discretization for high-order discontinuous Galerkin computations of tidal flows around shallow water islands. International Journal for Numerical Methods in Fluids 59, 535–557.

Blaise, S., St-Cyr, A., 2012. A Dynamic hp-Adaptive Discontinuous Galerkin Method for Shallow-Water Flows on the Sphere with Application to a Global Tsunami Simulation. Monthly Weather Review 140, 978–996.

Carter, G.S., Merrifield, M.A., 2007. Open boundary conditions for regional tidal simulations. Ocean Modelling 18, 194–209.

Cockburn, B., Shu, C., 1998. The local discontinuous Galerkin method for time-dependent convection-diffusion systems. Siam Journal on Numerical Analysis 35, 2440–2463.

Cockburn, B., Shu, C.W., 2002. Rungekutta discontinuous galerkin methods for convection-dominated problems. J. Sci. Comput. 16, 173–261.

Cools, R., 1999. Monomial cubature rules since Stroud: A compilation - part 2. Journal of Computational And Applied Mathematics 112, 21–27.

Cote, J., 1988. A lagrange multiplier approach for the metric terms of semi-lagrangian models on the sphere. Quarterly Journal of the Royal Meteorological Society 114, 1347–1352.
Dawson, C., Kubatko, E.J., Westerink, J.J., Trahan, C., Mirabito, C., Michoski, C., Panda, N., 2011. Discontinuous Galerkin methods for modeling Hurricane storm surge. Advances in Water Resources 34, 1165–1176.
Egbert, G., Bennett, A., Foreman, M., 1994. Topex/Poseidon tides estimated using a global inverse model. Journal of Geophysical Research-Oceans 99, 24821–24852.
Egbert, G., Ray, R., 2001. Estimates of tidal energy dissipation from TOPEX/Poseidon altimeter data. Journal of Geophysical Research 106, 22475–22502.
Egbert, G., Ray, R., 2003. Semi-diurnal and diurnal tidal dissipation from TOPEX/Poseidon altimetry. Geophysical Research Letters 30.
Egbert, G., Ray, R., Bills, B., 2004. Numerical modeling of the global semidiurnal tide in the present day and in the last glacial maximum. Journal of Geophysical Research-Oceans 109.
Eskilsson, C., Sherwin, S., 2004. A triangular spectral/hp discontinuous Galerkin method for modelling 2D shallow water equations. International Journal for Numerical Methods in Fluids 45, 605–623.
Farrell, W., 1972. Deformation of the Earth by Surface Loads. Reviews of Geophysics and Space Physics 10, 761–797.
Galewsky, J., Scott, R., Polvani, L., 2004. An initial-value problem for testing numerical models of the global shallow-water equations. Tellus Series A-Dynamic Meteorology and Oceanography 56, 429–440.
Garrett, C., Kunze, E., 2007. Internal tide generation in the deep ocean. Annual Review of Fluid Mechanics 39, 57–87.
Giraldo, F., 2000. Lagrange-Galerkin methods on spherical geodesic grids: The shallow water equations. Journal of Computational Physics 160, 336–368.
Giraldo, F., 2001. A spectral element shallow water model on spherical geodesic grids. International Journal for Numerical Methods in Fluids 35, 869–901.
Giraldo, F., 2006. High-order triangle-based discontinuous Galerkin methods for hyperbolic equations on a rotating sphere. Journal of Computational Physics 214, 447–465.
Giraldo, F., Hesthaven, J., Warburton, T., 2002. Nodal high-order discontinuous Galerkin methods for the spherical shallow water equations. Journal of Computational Physics 181, 499–525.
Gottlieb, S., Ketcheson, D., Shu, C., 2011. Strong Stability Preserving Runge-Kutta and Multistep Time Discretizations. World Scientific Publishing.
Gottlieb, S., Shu, C., 1998. Total variation diminishing Runge-Kutta schemes. Mathematics of Computation 67, 73–85.
Griffiths, S.D., Grimshaw, R.H.J., 2007. Internal tide generation at the continental shelf modeled using a modal decomposition: Two-dimensional results. Journal of Physical Oceanography 37, 428–451.
Griffiths, S.D., Peltier, W.R., 2008. Megatides in the Arctic Ocean under glacial conditions. Geophysical Research Letters 35.
Griffiths, S.D., Peltier, W.R., 2009. Modeling of Polar Ocean Tides at the Last Glacial Maximum: Amplification, Sensitivity, and Climatological Implications. Journal of Climate 22, 2905–2924.
Hendershott, M.C., 1972. The Effects of Solid Earth Deformation on Global Ocean Tides. Geophysical Journal International 29, 389–402.
Hesthaven, J.S., Warburton, T., 2008. Nodal discontinuous Galerkin methods: algorithms, analysis, and applications. Springer, New York.
Hill, D.F., Griffiths, S.D., Peltier, W.R., Horton, B.P., Toernqvist, T.E., 2011. High-resolution numerical modeling of tides in the western Atlantic, Gulf of Mexico, and Caribbean Sea during the Holocene. Journal of Geophysical Research-Oceans 116.
Ii, S., Xiao, F., 2010. A global shallow water model using high order multi-moment constrained finite volume method and icosahedral grid. Journal of Computational Physics 229, 1774–1796.
Jakobchien, R., Hack, J., Williamson, D., 1995. Spectral transform solutions to the shallow-water test set. Journal of Computational Physics 119, 164–187.
Karypis, G., Kumar, V., 1998. A fast and high quality multilevel scheme for partitioning irregular graphs. SIAM J. Sci. Comput. 20, 359–392.
Kelly, J.F., Giraldo, F.X., 2012. Continuous and discontinuous Galerkin methods for a scalable three-dimensional nonhydrostatic atmospheric model: Limited-area mode. Journal of Computational Physics 231, 7988–8008.
Kubatko, E.J., Bunya, S., Dawson, C., Westerink, J.J., 2009. Dynamic p-adaptive Runge-Kutta discontinuous Galerkin methods for the shallow water equations. Computer Methods in Applied Mechanics and Engineering 198, 1766–1774.
Laeuter, M., Giraldo, F.X., Handorf, D., Dethloff, K., 2008. A discontinuous Galerkin method for the shallow water equations in spherical triangular coordinates. Journal of Computational Physics 227, 10226–10242.
Le Provost, C., Genco, M., Lyard, F., Vincent, P., Canceil, P., 1994. Spectroscopy of the world ocean tides from a finite-element hydrodynamic model. Journal of Geophysical Research-Oceans 99, 24777–24797.
Logutov, O.G., Lermusiaux, P.F.J., 2008. Inverse barotropic tidal estimation for regional ocean applications. Ocean Modelling 25, 17–34.
Lyard, F., 1997. The tides in the Arctic ocean from a finite element model. Journal of Geophysical Research-Oceans 102, 15611–15638.
Lyard, F., Lefevre, F., Letellier, T., Francis, O., 2006. Modelling the global ocean tides: modern insights from FES2004. Ocean Dynamics 56, 394–415.
Munk, W., Wunsch, C., 1998. Abyssal recipes II: energetics of tidal and wind mixing. Deep-Sea Research Part I-Oceanographic Research Papers 45, 1977–2010.
Nair, R., Thomas, S., Loft, R., 2005. A discontinuous Galerkin global shallow water model. Monthly Weather Review 133, 876–888.
Nair, R., Thomas, S., Loft, R., 2005. A discontinuous Galerkin transport scheme on the cubed sphere. Monthly Weather Review 133, 814–828.
Peltier, W., Clark, T., 1979. Evolution and Stability of Finite-Amplitude Mountain Waves. Part II: Surface-Wave Drag and Severe Downslope Windstorms. Journal of the Atmospheric Sciences 36, 1498–1529.
Peltier, W., Clark, T., 1983. Non-linear mountain waves in 2 and 3 spatial dimensions. Quarterly Journal of the Royal Meteorological Society 109, 527–548.
Peltier, W., Scinocca, J., 1990. The Origin of Severe Downslope Windstorm Pulsations. Journal of the Atmospheric Sciences 47, 2853–2870.
Peltier, W.R., Drummond, R., Roy, K., 2012. Comment on Ocean mass from GRACE and glacial isostatic adjustment by D.P. Chambers et al. Journal of Geophysical Research-Solid, Earth 117.
Ray, R., 1998. Ocean self-attraction and loading in numerical tidal models. Marine Geodesy 21, 181–192.
Sadourny, R., Arakawa, A., Mintz, Y., 1968. Integration of the nondivergent barotropic vorticity equation with an icosahedral-hexagonal grid for the sphere. Mon. Wea. Rev 96, 351–356.
Smith, W., Sandwell, D., 1997. Global sea floor topography from satellite altimetry and ship depth soundings. Science 277, 1956–1962.
St-Cyr, A., Jablonowski, C., Dennis, J.M., Tufo, H.M., Thomas, S.J., 2008. A comparison of two shallow-water models with nonconforming adaptive grids. Monthly Weather Review 136, 1898–1922.
Stuhne, G., Peltier, W., 1999. New icosahedral grid-point discretizations of the shallow water equations on the sphere. Journal of Computational Physics 148, 23–58.
Stuhne, G., Peltier, W., 2006. A robust unstructured grid discretization for 3-dimensional hydrostatic flows in spherical geometry: A new numerical structure for ocean general circulation modeling. Journal of Computational Physics 213, 704–729.
Stuhne, G.R., Peltier, W.R., 2009. An unstructured C-grid based method for 3-D global ocean dynamics: Free-surface formulations and tidal test cases. Ocean Modelling 28, 97–105.
Taylor, G., 1919. Tidal friction in the Irish Sea. Proceedings of the Royal Society of London Series A-Containing Papers of a Mathematical and Physical Character 96, 330.
Thompson, J.F., editorSoni, B.K., editorWeatherhill, N.P. (Eds.), 1999. Handbook of Grid Generation. CRC Press.
Toro, E.F., 2001. Godunov Methods: Theory and Applications. Springer, New York.
Uehara, K., Scourse, J.D., Horsburgh, K.J., Lambeck, K., Purcell, A.P., 2006. Tidal evolution of the northwest European shelf seas from the Last Glacial Maximum to the present. Journal of Geophysical Research-Oceans 111.
Vallis, G.K., 2006. Atmospheric and Oceanic Fluid Dynamics. Cambridge University Press, Cambridge, U.K..
Wessel, P., Smith, W., 1996. A global, self-consistent, hierarchical, high-resolution shoreline database. Journal of Geophysical Research-Solid Earth 101, 8741–8743.
Williamson, D., Drake, J., Hack, J., Jakob, R., Swarztrauber, P., 1992. A standard test set for numerical approximations to the shallow-water equations in spherical geometry. Journal of Computational Physics 102, 211–224.